Journal of Molecular Structure 1334 (2025) 141859

Contents lists available at ScienceDirect

Journal of Molecular Structure

journal homepage: www.elsevier.com/locate/molstr

Small molecule regulation of iron homeostasis: design and optimization of novel iron chelators based on a thiosemicarbazone scaffold

Christian S. Parry [a,*], Yue Li [b], Samuel Kojo Kwofie [c], Josh Valencia [d], Cynthia A . Tope Niedermaier [d], Timothy R. Ramadhar [e], Sergei Nekhai [f], Michael D. Wilson [g], Raymond J. Butcher [e,*]

[a] Department of Microbiology, College of Medicine, Howard University, Washington, District of Columbia 20059. United States
[b] Department of Chemistry and Biochemistry, University of Maryland, College Park, Maryland 20742. United States
[c] Department of Biomedical Engineering, School of Engineering Sciences, College of Basic and Applied Sciences, University of Ghana, Legon, Accra LG 77. Ghana
[d] College of Natural and Mathematical Sciences, University of Maryland Baltimore County, 1000 Hilltop Circle, Baltimore, Maryland 21250. United States
[e] Department of Chemistry, College of Arts and Science, Howard University, Washington, District of Columbia 20059. United States
[f] Center for Sickle Cell Disease, Department of Medicine, Howard University, Washington District of Columbia 20060. United States
[g] Department of Parasitology, Noguchi Memorial Institute for Medical Research (NMIMR), College of Health Sciences (CHS), University of Ghana, Legon, Accra LG 581. Ghana

ARTICLE INFO

Keywords:
Aromatic heterocyclic ligands
Metal chelation
"soft" donor atoms
Highly reactive sulfur
Metal-based therapeutics

ABSTRACT

Disrupted iron balance causes anemia and iron overload leading to hypoxia and systemic oxidative stress. Iron overload may arise from red blood cell disorders such as sickle cell disease, thalassemia major and primary hemochromatosis, or from treatment with multiple transfusions. These hematological disorders are characterized by constant red blood cell hemolysis and the release of iron. Hemolysis is a continuous source of reactive oxygen species whose accumulation changes the redox potential in the erythrocyte, the endothelium and other tissue causing damage to organ systems. Iron overload and its consequences can be treated with iron chelating therapy. We have carried out structural studies of small molecule ligands that were previously reported for their iron chelating ability. The chelators were analyzed using mass spectrometry, proton nuclear magnetic resonance and infrared spectroscopy. The iron chelators, 2-benzoylpyridine-4,4-dimethyl-3-thiosemicarbazone, 3-ethyl-1-{[2-phenyl-1-(pyridin-2-yl)ethylidene]amino}thiourea and 1-{[2-phenyl-1-(pyridin-2-yl)ethylidene]amino}-3-(prop-2-en-1-yl)thiourea in their unbound conformation were crystallized and their structures were determined. This work addresses the evolution of a thiosemicarbazone class of iron chelators by analyzing and comparing the structure and properties of a series of closely related molecules, relating these to their *in vitro* activity thus providing valuable update to the search for newer, better and more effective iron chelators and metal-based therapeutics.

1. Introduction

Iron is essential for nearly all forms of life including mammals for whom iron is needed for red blood cell manufacture and hemoglobin production for oxygen transport. Additionally, iron is an essential co-factor in many enzymes that participate in a wide range of biological processes, such as electron transfer, DNA synthesis and metabolism. While iron is necessary for life, its excess can lead to toxicity through the production of highly reactive oxygen species such as peroxide ion (O_2^{-2}), superoxide anion radical ($O_2^{\bullet -}$) and hydroxyl radical ($OH^{\bullet}$) through the Fenton and Haber-Weiss reactions [1]. These prooxidant species induce oxidative stress causing damage to macromolecules, DNA, RNA, lipids and proteins, and leading to cellular injury, cell cycle arrest and senescence. Thus, it is necessary to maintain tight control of iron concentration and distribution.

Iron overload may arise in conditions of hemolytic anemias such as sickle cell disease, thalassemia major and hemochromatosis, multiple transfusions or liver diseases. Frequent hemolysis and disrupted iron balance may cause anemia, systemic iron overload and oxidative stress, and may further lead to chronic infection and debilitating disease [2].

* Corresponding authors.
E-mail addresses: christian.parry@Howard.edu (C.S. Parry), rbutcher@Howard.edu (R.J. Butcher).

https://doi.org/10.1016/j.molstruc.2025.141859
Received 3 June 2024; Received in revised form 17 February 2025; Accepted 23 February 2025
Available online 24 February 2025

Iron overload and oxidative stress affect nearly all organs with damage to the liver, heart and pancreas [3,4]. There is also growing appreciation that exposure to metals, and their resultant oxidative stress, are closely linked to many diseases, including Alzheimer's, Parkinson's, and Wilson's diseases [5,6]. Iron overload can be managed by iron chelation therapy [7,8]. The first iron chelators were siderophores and, currently, the most widely used chelating agent is desferrioxamine B (DFO) [9,10], an Fe(III)-selective hydroxamic acid-based molecule. DFO is hydrophilic and is poorly absorbed across the lipid membrane of the gastrointestinal tract. It requires a complicated administration protocol. Two other Fe (III) chelators, Deferasirox (DFX) and Deferiprone (DFP), have been developed and approved to treat complications associated with iron overload [7]. Both have high affinity for Fe(III) but noticeable side effects including kidney problems. There is a need for new chelators that are easy to administer and that have little or no side effects.

Following the work of Richardson [11], a previous collaboration [12,13] and our interest in natural products [14,15], we have chosen four progressively varying thiosemicarbazone based ligands with recognizable incremental changes – experimental iron chelators - to characterize in order to gain insight to their stereochemical properties and what makes them effective iron chelators. Their respective activity has been evaluated in *in vitro* and *in vivo* studies [16,17] but their structural features have not been completely characterized. The four ligands are: i) di-2-pyridylketone 4,4-dimethyl-3-thiosemicarbazone (Dp44mT; **L1**); ii) 2-benzoylpyridine-4,4-dimethyl-3-thiosemicarbazone (Bp44mT; **L2**); iii) 3-ethyl-1-{[2-phenyl-1-(pyridin-2-yl)ethylidene]amino}thiourea (PPYeT; **L3**); and iv) 1-{[2-phenyl-1-(pyridin-2-yl)ethylidene]amino}−3-(prop-2-en-1-yl)thiourea (PPYaT; **L4**). The structures of **L3** and **L4** are unknown. The search for selective and effective iron chelators without toxicity is a hard problem but one of fundamental and clinical importance [18]. Our broad strategy is to identify chemical groups that enhance properties that abrogate cellular iron and accompanying reactive oxidative species.

Thiosemicarbazones are organo-sulfur nitrogen-containing heterocycles with high affinity for metal binding [19–21]. They are found as natural products, have remarkable biological and chemical activity, are components of many biologically important molecules and are chemically and structurally versatile on account of their rich coordination modes - properties that make them good pharmacological leads. The thiosemicarbazone structure has characteristic azomethine, hydrazine and thioamide fragments that form an R2C═N–NR–C(═S)–NR2 backbone. **L1, L2, L3** and **L4**, are shown in Fig. 1.

L1 represents a well-known family of thiosemicarbazones with anti-ribonucleotide reductase activity. It has been used as an iron chelator but is also effective against a broad range of tumors [22]. **L1** analogs have been developed with greater cytotoxic and iron-chelating activity than DFO. **L1** carries out these effects through a dual mechanism: metal chelation and the formation of redox active metal complexes [23]. Another feature of **L1** is its ability to overcome resistance to established chemical treatments [24]. Significantly, **L1** is selective for tumor cells and does not kill normal tissue. But **L1** has cardiac side issues at nonoptimal doses [16]. The structure of L1 is known (PubChem CID 10334137), and **L1** has been replaced by new derivatives, di-2-pyridylketone 4-cyclohexyl-4-methyl-3-thiosemicarbazone (DpC) and 4-(pyridine-2-yl)-N-([(8*E*)−5,6,7,8-tetrahydroquinolin-8-ylidene] amino)piperazine-1-carbothioamide (COTI-2) [25]. For these reasons, we use **L1** only as a reference molecule.

L2 is derived from **L1** and involves a change from two pyridyl groups to one with the other pyridine replaced by a phenyl ring [16,26]. **L2** is more active and even more selective for tumor tissue than the predecessor **L1** molecules and does not have cardiac issues [16]. Further, **L2** can cross cell compartments more easily and can be administered orally. **L1** and **L2** inhibited HIV-1 transcription and replication by suppressing cell cycle-dependent kinase 2 (CDK2) and elevating HIV-1 inhibitory p21 [27,28]. A more recent study from the same group showed that newer derivatives of **L2** (**L3** and **L4**) are even more effective than **L2** in suppressing HIV-1 infection, through chelation, in cultured CEM T cells, promonocytic THP-1 cells, and in primary PBMCs without apparent toxicity as compared to DFO, **L1** or **L2** [17]. PBMCs are circulating white blood cells, B- and T- cells and NK cells, typified by a single round nucleus; CEM cells are a human immortal T cell line derived from a patient with acute lymphoblastic leukemia; THP-1 cells are a human immortal cell line derived from the peripheral blood of a patient with acute monocytic leukemia. The promising chelators, **L2, L3** and **L4**, have not been further characterized with respect to their structure. **L1, L2, L3** and **L4**, as TSCs, are expected to bind iron in a tridentate mode through pyridine N, azomethine N and the S moiety [19]. We report the comparative structural analyses of **L2, L3** and **L4**.

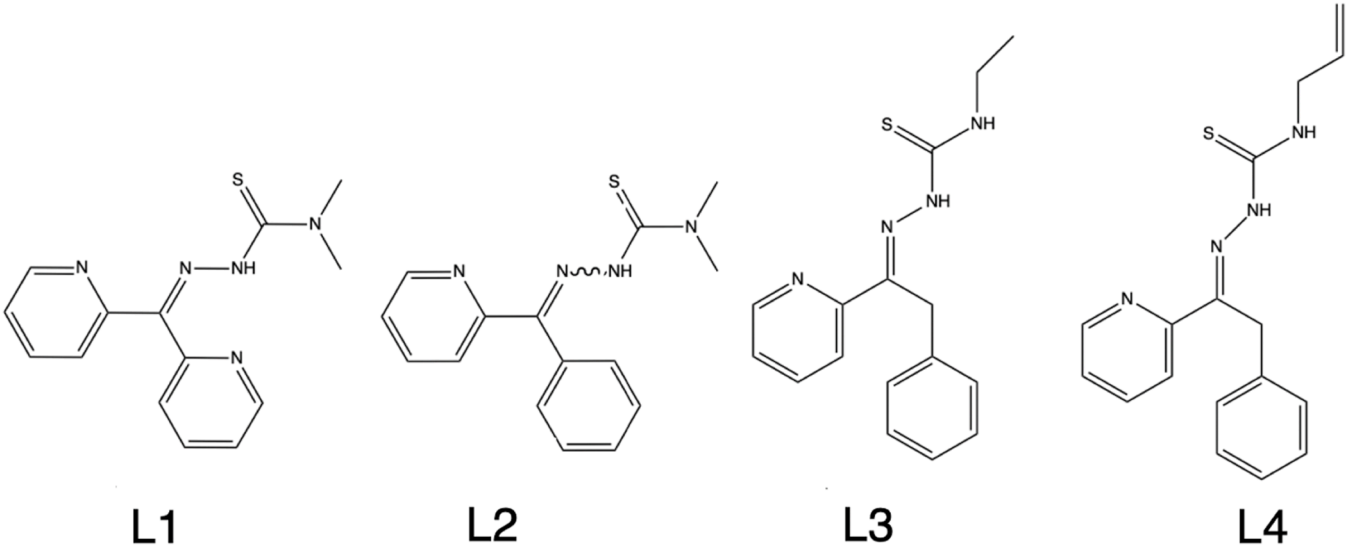

Fig. 1. The molecules we studying are: **L1**, di-2-pyridylketone 4,4-dimethyl-3-thiosemicarbazone; **L2**, 2-benzoylpyridine-4,4-dimethyl-3-thiosemicarbazone; **L3**, 3-ethyl-1-{[2-phenyl-1-(pyridin-2-yl)ethylidene]amino}thiourea; and **L4,** 1-{[2-phenyl-1-(pyridin-2-yl)ethylidene]amino}−3-(prop-2-en-1-yl)thiourea. **L1** is chosen as the reference structure and represents the parent thiosemicarbazone frame.

2. Experimental

2.1. Materials and methods

The ligands **L2** (2-benzoylpyridine-4,4-dimethyl-3-thiosemicarbazone), **L3** (3-ethyl-1-{[2-phenyl-1-(pyridin-2-yl)ethylidene] amino}thiourea) and **L4** (1-{[2-phenyl-1-(pyridin-2-yl)ethylidene]amino}−3-(prop-2-en-1-yl)thiourea) were synthesized for us by Enamine (Monmouth Junction, NJ) by custom order. We carried out mass spectrometry (MS), proton nuclear magnetic resonance (1H—NMR) spectroscopy and infrared (IR) spectroscopy analyses.

For each sample, **L2, L3** and **L4**, 5 mg of the compound in powder form was dissolved in 1 ml acetonitrile. An atmospheric pressure ionization time-of-flight (TOF) mass spectrometer (AccuTOF, JEOL, USA, Inc.) equipped with an electrospray ionization (ESI) ion source was coupled with an Agilent 1100 HPLC system and used in electrospray ionization mass spectrometry (ESI–MS) analysis based on direct infusion. The AccuTOF MS settings were as follows: orifice 1 temperature = 80 °C; orifice 1 voltage, V = 30 V, orifice 2 voltage = 5 V, and ring voltage = 10V. The desolvation chamber temperature was set at 250 °C, and the flow rates of the nebulizing and desolvation gases were set to 0.6 and 3.0 l/min, respectively. Mass spectra were acquired in the positive mode at a rate of one spectrum per second within the mass-to-charge ratio (m/z) range of 100–700. Sample injection volume was 10 µl. Calibration for exact mass measurement was carried out using polyethylene glycol (average molecular weight = 600) as internal standard.

The three samples **L2, L3** and **L4** were dissolved in deuterated acetonitrile (acetonitrile-d_3; CD_3CN), acetone ($CD_3C{=}OCD_3$; acetone-d_6), and acetonitrile, respectively. 1D ^{1}H NMR analysis was conducted using a 500 MHz Bruker AvanceIII HD (Bruker Corporation, Billerica, MA) instrument equipped with a TBI (**T**riple resonance **B**roadband +*X* Decoupling, **I**nverse ^{1}H) probe maintained through the experiment at 20 °C. We collected spectra from −4 to 16 ppm, with a relaxation delay of three seconds. 32 scans were accumulated. Baseline and phase of spectra were corrected using the MNova processing software from MestreLab Research (Bruker Corporation). After this, peaks were picked and integrated using MNova. Spectra were referenced by solvent.

Infrared analysis was conducted using a PerkinElmer Frontier IR spectrometer with a UATR sampling system and a ZnSe crystal. For each sample spectra were collected from 4000 to 650 cm^{-1} for a total of 16 scans. Peaks of each spectra set were labeled using the PerkinElmer

Spectrum software. Data is reported to an accuracy of 0.01 cm-1.

2.2. Single crystal X-ray crystallography

Crystallization trials by vapor diffusion were conducted using acetone or acetonitrile as solvents, and ether or dichloromethane as precipitants. After crystals have formed, they were harvested from the vial, placed on a slide in a drop of oil and trimmed. We used a wand with a loop at the tip to collect a single crystal to place on a mount. The mount was placed on the 4-circle goniometer and centered. Diffraction data was collected from a Rigaku Oxford Synergy S Dual Source Single Crystal Diffractometer (Rigaku USA, The Woodlands, TX) driven by CrysAlisPro (Oxford Diffraction, Yarnton UK). The X-ray radiation source was copper (Cu Kα1, wavelength=1.54184 Å). The crystal was typically kept at 100 K in a stream of liquid nitrogen (LN2) supplied by an Oxford Cryosystream unit (Oxford Cryosystems, Oxford, UK), when available, for low-temperature measurements. Diffraction intensity was collected on a HYPIX 6000HE Detector (Rigaku USA, The Woodlands, TX) for rapid non-shutter operation. After a short pre-experiment run a complete reflection data set was collected in *kappa* mode. Collected X-ray reflection data was integrated and finalized in CrysAlisPro. The structure was solved by intrinsic phasing using SHELXT [29] and refined with SHELXL [30,31] running under Olex2–1.5 [32]. Olex2–1.5 was used as an interface for control, general analysis and visualization.

3. Results and discussion

3.1. Spectral characterization of L2, L3 and L4

The mass spectra of the three samples were obtained in ESI positive mode. The spectra are shown in Supplementary Figure S1. The three compounds were identified from their spectra as protonated ions at m/z = 285.1174, 299.1327 and 311.1325, respectively. The latter two values ($M + H = 299.1327$ and $M + H = 311.1325$), corresponding to **L3** and **L4**, match precisely values previously reported by Kumari et al. ($M + H = 299.1332$ and $M + H = 311.1328$) [17].

Proton nuclear magnetic resonance spectra of the samples are given below:

Ligand **L2** (2-benzoylpyridine-4,4-dimethyl-3-thiosemicarbazone) -

^{1}H NMR (500 MHz, CD_3CN) δ 14.81 ppm (s, 1H), 8.80 ppm (ddd, *J* = 4.9, 1.9, 1.0 Hz, 1H), 7.90 ppm (td, *J*= 7.9, 1.8 Hz, 1H), 7.57 – 7.53 ppm (m, 2H), 7.51 – 7.45 ppm (m, 4H), 7.35 ppm (dt, *J*= 8.0, 1.0 Hz, 1H), 3.40 ppm (s, 6H).

Ligand **L3** (3-ethyl-1-{[2-phenyl-1-(pyridin-2-yl)ethylidene]amino} thiourea) -

^{1}H NMR (500 MHz, Acetone) δ 14.34 ppm (s, 1H), 8.76 ppm (ddd, *J* = 4.8, 1.9, 0.9 Hz, 1H), 8.35 ppm (s, 1H), 7.94 ppm (td, *J* = 7.9, 1.8 Hz, 1H), 7.76 ppm (d, *J* = 8.2 Hz, 1H), 7.47 ppm (ddd, *J* = 7.6, 4.9, 1.1 Hz, 1H), 7.35 ppm (d, *J* = 6.8 Hz, 2H), 7.29 ppm (t, *J* = 7.7 Hz, 2H), 7.23 – 7.18 ppm (m, 1H), 4.14 (s, 2H), 3.70 ppm (qd, *J* = 7.2, 5.7 Hz, 2H), 1.21 ppm (t, *J* = 7.2 Hz, 3H).

Ligand **L4** (1-{[2-phenyl-1-(pyridin-2-yl)ethylidene]amino}−3-(prop-2-en-1-yl)thiourea) -

^{1}H NMR (500 MHz, CD_3CN) δ 14.45 ppm (s, 1H), 8.73 ppm (ddd, *J* = 4.9, 1.9, 0.9 Hz, 1H), 8.18 ppm (s, 1H), 7.89 ppm (td, *J* = 7.9, 1.8 Hz, 1H), 7.69 ppm (d, *J* = 8.2 Hz, 1H), 7.43 ppm (ddd, *J* = 7.7, 4.9, 1.1 Hz, 1H), 7.33 ppm (dt, *J* = 15.2, 7.3 Hz, 4H), 7.27 – 7.20 ppm (m, 1H), 5.98 ppm (ddt, *J* = 17.2, 10.5, 5.4 Hz, 1H), 5.27 – 5.12 ppm (m, 2H), 4.32 ppm (tt, *J* = 5.6, 1.7 Hz, 2H), 4.15 ppm (s, 2H).

The data above is also shown in Figure S2 with the ligand structures mapped to their respective spectra. For example, in ligand **L2**: 1H NMR (500 MHz, CD3CN) δ 14.81 (s, 1H) corresponds to NH; 8.80 (ddd, *J* = 4.9, 1.9, 1.0 Hz, 1H) corresponds to pyridinic proton ortho to N; 7.90 (td, *J* = 7.9, 1.8 Hz, 1H) corresponds to phenyl ring para protons; 7.57 – 7.53 (m, 2H) correspond to pyridinic proton meta and para to N; 7.51 – 7.45 (m, 4H) correspond to phenyl ring meta and ortho protons. Pyridinic proton ortho to the N, 7.35 (dt, *J* = 8.0, 1.0 Hz, 1H) corresponds to pyridinic proton ortho to methyl substituent; and 3.40 (s, 6H) corresponds to the two methyl groups on N.

We collected infrared transmittance data from wavenumbers 4000 cm^{-1} to 650 cm^{-1} (Supplementary Figure S3). For ligand **L2** (2-benzoylpyridine-4,4-dimethyl-3-thiosemicarbazone), five absorption bands show up clearly in the first region of interest (4000 cm^{-1} to 2500 cm^{-1}), the single bond region: 3052, 3024, 2993, 2921 and 2852 cm^{-1}). Bands at 3052 cm^{-1} and 3024 cm^{-1} are characteristic of N—H stretching of primary amines and 2993 cm^{-1} represents the C—H stretching of sp3 carbon (methyl). The peak at 1578 cm^{-1} is assigned to C=N; and N—H vibration is assigned at 3052 cm^{-1}. There is a weak absorption band at 2221 cm^{-1}. We attribute this and the next set of absorption bands to vibrational overtones from the aromatic rings in the sample. The characteristic C=S stretching band is assigned to the peak at 1116 cm^{-1}. This is consistent with previous assignments to bands in the region 1130–1080 cm^{-1} to C=S vibration. The peak at 1578 cm^{-1} is assigned to C=N; and N—H vibration is assigned at 3052 cm^{-1}. Similarly, for ligand L3 (3-ethyl-1-{[2-phenyl-1-(pyridin-2-yl)ethylidene]amino}thiourea), C=S vibration is thought to be the strong band at 1103 cm^{-1}. Corresponding peak to the C=N group is 1587 cm^{-1}; and the NH group is thought to be at 3173 cm^{-1}.

There is a band at 1644 cm^{-1} that may be attributed to -C═CH2 of ligand **L4**; it is not present in either **L3** or **L2**.

3.2. Single crystal crystallography

Crystals typically grew from solvent over a few days to several weeks. Ligand **L2** was readily soluble in acetonitrile and similar polar solvents. **L4** was similarly soluble but **L3** was poorly soluble in acetonitrile. **L3** crystallized in acetone and benzene. Suitable crystals of **L3** also formed after a few months from the same solvents by liquid diffusion and slow evaporation. A summary of crystallographic parameters is presented in Table 1.

L2 ($C_{15}H_{16}N_4S$) lies in an extended conformation, in this view (Fig. 2A), with the two aromatic rings at the bottom and the thiosemicarbazone stem pointing up. Both the pyridine ring (formed by atoms C6, C2, C3, C5 N1, C4) and phenyl ring (atoms C16, C20, C19, C17, C15, C18) are planar (Fig. 2A): respective root mean squared atom to plane deviation are 0.008 Å and 0.001 Å, respectively, but the planes are not coplanar. The angle between the two planes is 60.17(4)° with plane centroid to plane centroid distance of 5.0111(7) Å.

Bond length values in bonds C7-C15 and C7-C2 (1.4976 Å and 1.4887 Å, respectively) are notably different from the bond length values in bonds such as C15-C16 and C19-C20 (1.3939 Å and 1.3920 Å, respectively). Bonds C15-C16 and C19-C20 are carbon-carbon bonds within the aromatic benzene ring. These bond length values are typically 1.39 Å and are significantly different from a regular -C-C- bond length value (1.54 Å) (sigma to sigma bonding). Bond length values in bonds C7-C15 and C7-C2 (1.4976 Å and 1.4887 Å, respectively) are still quite smaller than a regular C—C bond (Fig. 2A). This deviation may be accounted for in that the carbon atoms that form bonds C7-C15 and C7-C2 are next to or are part of atoms with either delocalized electrons or unsaturated orbitals.

A hydrogen bond is formed between the hydrazine nitrogen (N9) and pyridine nitrogen N1 and is the only hydrogen bond in the structure. There is further electron delocalization over the hydrazine group (N1, N2), sulfur (S1) and the farthest nitrogen (N3) making the stem of the ligand (C12, N1, N2, C13, S1, N3) and the pyridine ring to lie in the same plane. Bond C10-S is long (1.686 Å) and sulfur atom S is *trans* to the pyridine ring. A similar structure has been reported but is a semicarbazone and lacks the sulfur [33].

In ligand **L3** ($C_{16}H_{18}N_4S$), there is a hydrogen bond between pyridine ring nitrogen N4 and the hydrazine N (N2). Otherwise, the molecule is in an extended conformation with the aromatic rings forming the bottom (base) of the molecule, and the stem extending upward from the base as in **L2**. The thiosemicarbazone core is flat and coplanar with the pyridine ring. Unlike in **L2, L3** sulfur atom S is *cis* to pyridine N (Fig. 2B).

A benzyl ring has replaced the phenyl ring. Root mean deviation of pyridine ring atoms from planarity is 0.004 Å; the corresponding value for the benzene ring is similarly 0.004 Å. The angle between the planes of the two rings is 81.70(8)° with plane centroid to plane centroid distance of 5.1900(14) Å.

As with **L2** and **L3**, the **L4** thiosemicarbazone core and the pyridine ring lie in the same plane. **L4** phenyl ring is markedly rotated. The phenyl ring is about perpendicular to the plane of the pyridine and is swung about the benzyl ring toward the stem of the molecule. There is a dihedral angle of 98.46(8)° between the planes of the pyridine ring and the benzyl ring, twist angle of 97.83(5)°, fold angle 20.19(8)°, and plane centroid to plane centroid distance of 6.5816(9) Å. There is a hydrogen bond between pyridine nitrogen (N17) and TSC hydrazine nitrogen N10. This hydrogen bond is conserved in all three molecules.

The tip of the stem of the thiosemicarbazone group makes a perpendicular turn and bends downward toward the benzyl ring. This is aided energetically by an ethyl hydrogen in a putative CH-pi bond between the stem of the ligand and the benzyl ring. These effects are shown in Fig. 2D, in a superposition of ligand **L4** on ligand **L3**. Also, **L3** and **L4** have a -CH2- extension to the phenyl group, the benzyl group offering an additional dimension of conformational freedom compared to **L2** (Fig. 1).

Table 1
Summary of X-ray structure determination. Statistics and summary of structure determination and refinement for molecules **L2, L3** and **L4**.

Molecule	L2	L3	L4
Empirical formula	$C_{15}H_{16}N_4S$	$C_{16}H_{18}N_4S$	$C_{17}H_{18}N_4S$
Formula weight g/mol	284.38	298.40	310.41
Temperature/K	100.15	296.15	100.10
Crystal system	Monoclinic	Monoclinic	Triclinic
Space group	$P2_1/c$	$P2_1/c$	P-1
a/Å	17.24347(12)	8.6254(3)	8.78260(10)
b/Å	5.83811(4)	19.2454(5)	8.90510(10)
c/Å	13.80804(8)	10.1401(3)	10.9967(2)
α/°	90	90	80.2580(10)
β/°	93.3252(6)	109.383(4)	75.8560(10)
γ/°	90	90	68.0790(10)
Volume/Å^3	1387.704(15)	1587.84(9)	770.77(2)
Z	4	4	2
$^3_{\rho calcg/cm}$	1.361	1.248	1.338
μ/mm^{-1}	2.024	1.792	1.869
F(000)	600.0	632.0	328.0
Crystal size/mm^3	0.05 × 0.025 × 0.2	0.05 × 0.05 × 0.15	0.10 × 0.05 × 0.05
Radiation	CuKα (λ = 1.54184)	CuKα (λ = 1.54184)	CuKα (λ = 1.54184)
2Θ range for data collection/°	5.134 to 152.238	9.19 to 151.952	8.324 to 152.306
Index ranges	$-21 \le h \le 21$, $-4 \le k \le 7$, $-17 \le l \le 17$	$-10 \le h \le 10$, $-22 \le k \le 24$, $-8 \le l \le 12$	$-11 \le h \le 9$, $-11 \le k \le 10$, $-13 \le l \le 13$
Reflections collected	25,301	10,667	14,580
Independent reflections	2842 [R_{int} = 0.0385, R_{sigma} = 0.0204]	3184 [R_{int} = 0.0387, R_{sigma} = 0.0386]	3103 [R_{int} = 0.0377, R_{sigma} = 0.0271]
Data/restraints/parameters	2842/0/183	3184/0/191	3103/0/211
Goodness-of-fit on F^2	1.062	1.096	1.084
Final R indexes [I>=2σ (I)]	R_1 = 0.0302, wR_2 = 0.0803	R_1 = 0.0444, wR_2 = 0.1197	R_1 = 0.0346, wR_2 = 0.0902
Final R indexes [all data]	R_1 = 0.0313, wR_2 = 0.0814	R_1 = 0.0548, wR_2 = 0.1348	R_1 = 0.0396, wR_2 = 0.0999
Largest diff. peak/hole / e Å^{-3}	0.27/−0.26	0.27/−0.25	0.26/−0.34

3.3. Discussion

The search for newer and more effective iron chelators with little or no side effects remains an outstanding problem. Like siderophores, the four molecules in this study have been shown to have great affinity and selectivity for iron. Siderophores, exemplified by catecholates, hydroxamates and hydroxycarboxylates, possess “hard donor” groups, typically involving oxygen, for tight interaction with metal centers. The metal binding chemical units have donor atoms with lone pairs to facilitate rich coordination chemistry with the hard Lewis acid of metals, usually, transition metals. The widely used chelator Desferrioxamine (DFO) binds iron strongly as Fe(III). Similarly, **L1, L2, L3** and **L4**, as iron chelating agents, are expected to bind iron strongly. In contrast to siderophore complexes with metals, however, studies on the constants of formation of TSCs with metals, including iron are hard to come by. TSCs bind iron tightly in both its Fe(II) and Fe(III) oxidation states [34,35]. This is a key property of thiosemicarbazone ligands. TSCs have the useful characteristic as potent chelating agents that can remove iron ions regardless of their charge state: whether in the Fe(II) state or Fe(III) state, Fe strongly prefers an octahedral coordination geometry. Thus, in an Fe-ligand complex, two thiosemicarbazone ligands bind one Fe atom to complete the 6-coordination complex. Likewise, since both Fe(II) and Fe(III) prefer to bind in an octahedral conformational mode, Fe is able to cycle rapidly between the two states. Fe in Fe-thiosemicarbazone complexes is redox active. Cycling between the two states can generate reactive oxygen species (ROS), a property that is exploited in research

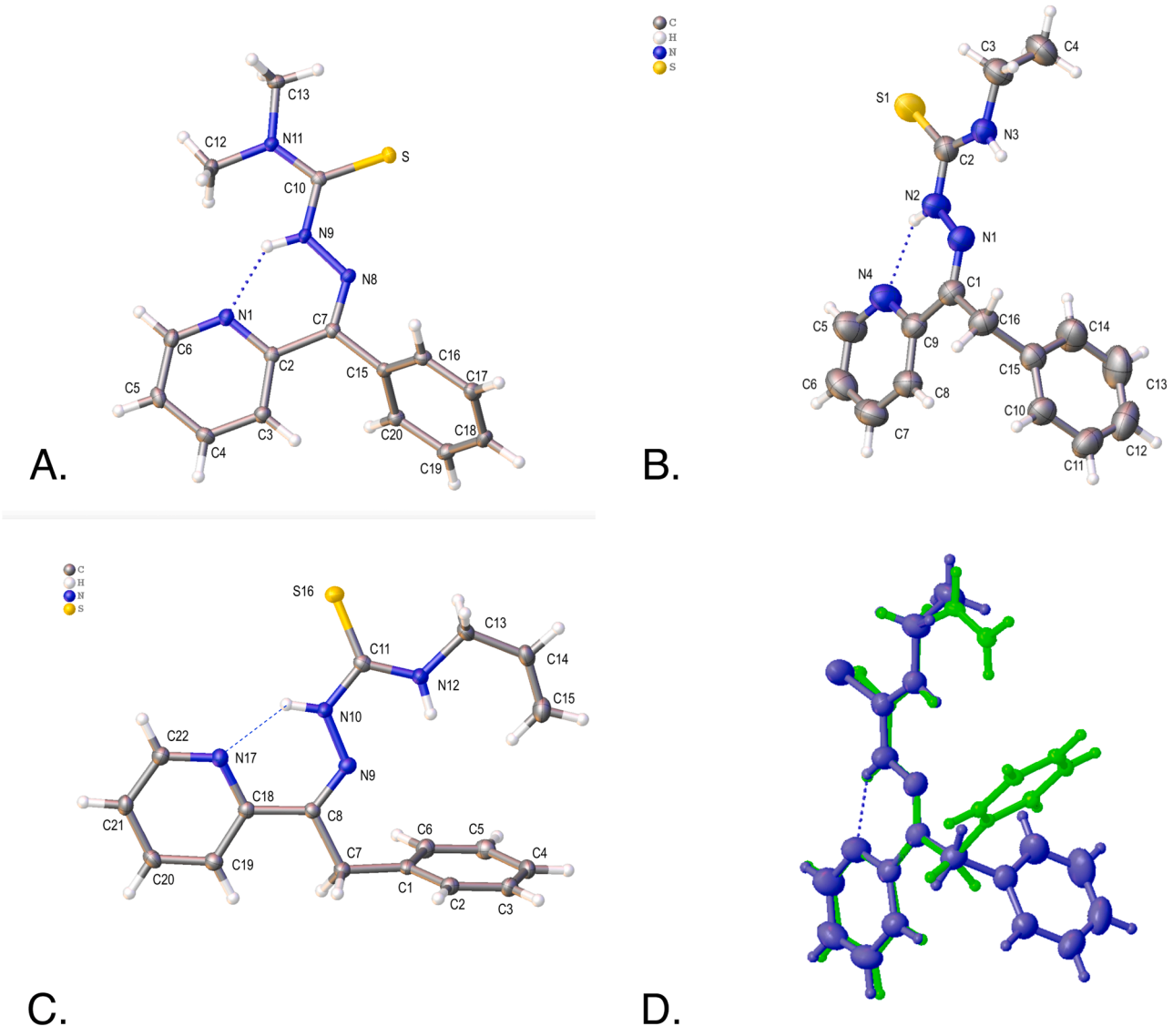

Fig. 2. Crystal structures of the chelators in their unbound form. Ligands **L2, L3**, and **L4** lie in an extended conformation. There is a conserved hydrogen bond between pyridine N and hydrazine N. **A.** The thio group in **L2** lies *trans* across the stem away from the pyridine ring. **B.** The thio group in **L3** lies *cis* to the pyridine ring. **C.** The stem of **L4** makes a downward turn for a CH group to make a CH-pi interaction with benzene's aromatic ring. **D.** shows an overlay of the closely related molecules **L3** and **L4. L3** is shown in dark blue/purple and **L4** is lime green.

pertaining to cancer treatment, in specific cell killing [34].

The transition between the two redox states makes the distinction between Fe(II) and Fe(III) compounds difficult. Related to this, thione-thiol tautomerism in thiosemicarbazone compounds are well documented [19]. This appears to be an intrinsic property of thiosemicarbazone ligands. It is evident in and shown to be important in copper(II) binding to Dp44mT (L1), particularly, as it pertains to the production of reduced oxygen species [36].

The crystal structures of **L2, L3** and **L4** confirm the thione tautomer in our ligands. We also obtained a crystal structure of L2 bound with iron. The structure showed two ligands binding to a single Fe(III) ion, accompanied by a $(FeCl_4)^-$ species, ie. $[Fe(III)(L2)_2]^+[Fe(III)Cl_4]^-$ where L2′ is singly deprotonated L2 ligand (Parry, unpublished data). These substantiate the thione state and the ligand preference for Fe(III). In the crystallization trials, we added equimolar amounts of L2 (dissolved in acetonitrile) and iron ($Fe(III)Cl_3$). We let the reaction sit for 20 mins. We used this reaction without transfer for crystallization by vapor diffusion placing the reaction vial in a larger vial containing diethyl ether as precipitant. The reaction vial was left uncapped and the larger (precipitant) vial was capped.

We were not able to detect thiol formation in our NMR experiments and we have not pursued this further.

4. Conclusion

These studies have revealed structural characteristics of three model ligands **L2, L3** and **L4** by mass spectrometry, NMR and infrared spectroscopy and X-ray crystallography, yielding complementary information that are likely to be useful in designing and optimizing small molecule leads. We found it remarkable that a small aliphatic extension to **L2** resulting in **L3** (a phenyl ring to a benzyl ring) produced a markedly different polar/hydrophobic profile to **L3**. This overall hydrophobic characteristic is reversed in **L4** with the addition of the sp^2 C = H_2 tip. The structure of **L4** demonstrates the dual role of weak intramolecular bonds (CH-pi) and conformational accessibility - from the addition of an ethyl group, with its unsaturated bonds and the introduction of the benzyl ring. The latter adds an extra degree of freedom that brings in the *pi* cloud of the benzyl group that can interact

favorably with the induced polar group from the ethene tip. The Richardson group observed that in studies in mice, administration of Dp44mT (**L1**) at non-optimal doses led to cardiac issues [16] but this was alleviated for Bp44mT (**L2**). We attribute this improved clinical characteristic of **L2** to the replacement of the second pyridine in **L1** to a benzene ring, and the release of the hydrogen bond that latched the replaced pyridine.

Thiosemicarbazone ligands, either by themselves or bound by metal, show pharmaceutical promise [37,38]. Thiosemicarbazone ligands and complexes can be designed with the redox potential tuned to deliver desired properties [39]. These and the rich stereochemical properties of this class of molecules suggest possibilities of metal-based organic ligands for pharmacological purposes. **L2, L3** and **L4** have shown promise in use as antivirals in studies with mice [17,28]. The understanding gained form these studies may lead to new modification for potential development as experimental therapeutics for iron overload disorders and microbe-based illnesses.

Supplementary data

Supplementary Figure **S1**. The mass spectra of **L2, L3** and **L4** are shown. Peaks corresponding to **L2, L3** and **L4** were identified from the spectra at $m/z = 285.1174$, 299.1327 and 311.1325, respectively.

Supplementary Figure **S2.** Proton nuclear magnetic resonance peaks are plotted for **L2, L3**, and **L4** in panels A, B, and C, respectively. The peaks are assigned accordingly.

Supplementary Figure **S3.** Infrared spectroscopy. Infrared transmittance data from **L2, L3** and **L4** covering wavenumbers 4000 cm^{-1} to 650 cm^{-1} are shown in panels A, B and C, respectively. Bands are consistent with the expected structures and features of the molecules.

CRediT authorship contribution statement

Christian S. Parry: Writing – review & editing, Writing – original draft, Visualization, Validation, Resources, Investigation, Funding acquisition, Formal analysis, Data curation, Conceptualization. **Yue Li:** Writing – review & editing, Visualization, Validation, Resources, Investigation, Formal analysis. **Samuel Kojo Kwofie:** Writing – review & editing, Validation, Software, Investigation. **Josh Valencia:** Writing – review & editing, Validation, Methodology, Investigation, Formal analysis. **Cynthia A . Tope Niedermaier:** Supervision, Resources, Investigation. **Timothy R. Ramadhar:** Writing – review & editing, Validation, Investigation. **Sergei Nekhai:** Writing – review & editing, Investigation. **Michael D. Wilson:** Writing – review & editing, Investigation, Conceptualization. **Raymond J. Butcher:** Writing – review & editing, Visualization, Validation, Supervision, Resources, Methodology, Investigation, Formal analysis, Conceptualization.

Declaration of competing interest

The authors declare that they have no known competing financial interests or personal relationships that could have appeared to influence the work reported in this manuscript.

Acknowledgements

We gratefully thank: Howard University College of Medicine for funding and support (Project U100272, Fund# 19, Program# 02); and NSF MRI grant (DMR-2117502) for the X-ray diffractometer.

Supplementary materials

Supplementary material associated with this article can be found, in the online version, at doi:10.1016/j.molstruc.2025.141859.

Data availability

All data used in this work will be made available upon request. CCDC accession numbers 2358773, 2358774 and 2358777 contain the supplementary crystallographic data for this paper. These data can be obtained free via http://www.ccdc.cam.ac.uk/conts/retrieving.html

References

[1] K. Jomova, R. Raptova, S.Y. Alomar, S.H. Alwasel, E. Nepovimova, K. Kuca, M. Valko, Reactive oxygen species, toxicity, oxidative stress, and antioxidants: chronic diseases and aging, Arch Toxicol 97 (2023) 2499–2574.
[2] G.J. Kato, M.H. Steinberg, M.T. Gladwin, Intravascular hemolysis and the pathophysiology of sickle cell disease, J Clin Invest 127 (2017) 750–760.
[3] E.J. van Beers, Y. Yang, N. Raghavachari, X. Tian, D.T. Allen, J.S. Nichols, L. Mendelsohn, S. Nekhai, V.R. Gordeuk, J.G. Taylor, G.J. Kato, Iron, inflammation, and early death in adults with sickle cell disease, Circ Res 116 (2015) 298–306.
[4] Q. Wang, R. Zennadi, The role of RBC oxidative stress in sickle cell disease: from the molecular basis to pathologic implications, Antioxidants (Basel) 10 (2021) 1608.
[5] M.P. Gotsbacher, T.J. Telfer, P.K. Witting, K.L. Double, D.I. Finkelstein, R. Codd, Analogues of desferrioxamine B designed to attenuate iron-mediated neurodegeneration: synthesis, characterisation and activity in the MPTP-mouse model of Parkinson's disease, Metallomics 9 (2017) 852–864.
[6] K.L. Summers, K.M. Schilling, G. Roseman, K.A. Markham, N.V. Dolgova, T. Kroll, D. Sokaras, G.L. Millhauser, I.J. Pickering, G.N. George, X-ray absorption spectroscopy investigations of copper(II) coordination in the Human amyloid β peptide, Inorg Chem 58 (2019) 6294–6311.
[7] A.V. Hoffbrand, A. Taher, M.D. Cappellini, How I treat transfusional iron overload, Blood 120 (2012) 3657–3669.
[8] T.D. Coates, J.C. Wood, How we manage iron overload in sickle cell patients, Br J Haematol 177 (2017) 703–716.
[9] J.A. Garibaldi, J.B. Neilands, Formation of iron-binding compounds by microorganisms, Nature 177 (1956) 526–527.
[10] H. Bickel, R. Bosshardt, E. Gaumann, P. Reusser, E. Vischer, W. Voser, A. Wettstein, H. Zahner, Stoffwechselprodukte von Actinomyceten. 26. Uber die isolierung und charakterisierung der ferrioxamine A-F, neuer wuchsstoffe der sideramin-gruppe, Helv. Chim. Acta 43 (1960) 2118–2128.
[11] D.S. Kalinowski, D.R. Richardson, The evolution of iron chelators for the treatment of iron overload disease and cancer, Pharmacol Rev 57 (2005) 547–583.
[12] A. Walcourt, M. Loyevsky, D.B. Lovejoy, V.R. Gordeuk, D.R. Richardson, Novel aroylhydrazone and thiosemicarbazone iron chelators with anti-malarial activity against chloroquine-resistant and -sensitive parasites, Int J Biochem Cell Biol 36 (2004) 401–407.
[13] A. Walcourt, J. Kurantsin-Mills, J. Kwagyan, B.B. Adenuga, D.S. Kalinowski, D. B. Lovejoy, D.J. Lane, D.R. Richardson, Anti-plasmodial activity of aroylhydrazone and thiosemicarbazone iron chelators: effect on erythrocyte membrane integrity, parasite development and the intracellular labile iron pool, J Inorg Biochem 129 (2013) 43–51.
[14] O. Agyapong, S.O. Asiedu, S.K. Kwofie, W.A. Miller, C.S. Parry, R.A. Sowah, M. D. Wilson, Molecular modelling and de novo fragment-based design of potential inhibitors of beta-tubulin gene of Necator americanus from natural products, Inform Med Unlocked 26 (2021) 100734.
[15] L.K.S. Darko, E. Broni, D.S.Y. Amuzu, M.D. Wilson, C.S. Parry, S.K. Kwofie, Computational study on potential novel anti-ebola virus protein VP35 natural compounds, Biomedicines 9 (2021) 1796.
[16] Y. Yu, Y. Suryo Rahmanto, D.R. Richardson, Bp44mT: an orally active iron chelator of the thiosemicarbazone class with potent anti-tumour efficacy, Br J Pharmacol 165 (2012) 148–166.
[17] N. Kumari, S. Iordanskiy, D. Kovalskyy, D. Breuer, X. Niu, X. Lin, M. Xu, K. Gavrilenko, F. Kashanchi, S. Dhawan, S. Nekhai, Phenyl-1-pyridin-2yl-ethanone-based iron chelators increase iκb-α expression, modulate CDK2 and CDK9 activities, and inhibit HIV-1 transcription, Antimicrob Agents Chemother 58 (2014) 6558–6571.
[18] R.C. Hider, X. Kong, Chemistry and biology of siderophores, Nat Prod Rep 27 (2010) 637–657.
[19] T.S. Lobana, R. Sharma, G. Bawa, S. Khanna, Bonding and structure trends of thiosemicarbazone derivatives of metals—An overview, Coordination Chemistry 253 (2009) 977–1055.
[20] Y. Yu, D.S. Kalinowski, Z. Kovacevic, A.R. Siafakas, P.J. Jansson, C. Stefani, D. B. Lovejoy, P.C. Sharpe, P.V. Bernhardt, D.R. Richardson, Thiosemicarbazones from the old to new: iron chelators that are more than just ribonucleotide reductase inhibitors, J Med Chem 52 (2009) 5271–5294.
[21] T.S. Lobana, S. Khanna, R.J. Butcher, 2-Benzoylpyridine thiosemicarbazone as a novel reagent for the single pot synthesis of dinuclear Cu I–Cu II complexes: formation of stable copper (ii)–iodide bonds, Dalton Transactions 41 (2012) 4845–4851.
[22] P.J. Jansson, P.C. Sharpe, P.V. Bernhardt, D.R. Richardson, Novel thiosemicarbazones of the ApT and DpT series and their copper complexes: identification of pronounced redox activity and characterization of their antitumor activity, J Med Chem 53 (2010) 5759–5769.
[23] Z. Kovacevic, D.S. Kalinowski, D.B. Lovejoy, P. Quach, J. Wong, D.R. Richardson, Iron chelators: development of novel compounds with high and selective anti-tumour activity, Curr Drug Deliv 7 (2010) 194–207.
[24] J. Yuan, D.B. Lovejoy, D.R. Richardson, Novel di-2-pyridyl-derived iron chelators with marked and selective antitumor activity: *in vitro* and *in vivo* assessment, Blood 104 (2004) 1450–1458.

[25] P. Heffeter, V.F.S. Pape, É.A. Enyedy, B.K. Keppler, G. Szakacs, C.R. Kowol, Anticancer thiosemicarbazones: chemical properties, interaction with iron metabolism, and resistance development, Antioxid Redox Signal 30 (2019) 1062–1082.
[26] D.S. Kalinowski, Y. Yu, P.C. Sharpe, M. Islam, Y.T. Liao, D.B. Lovejoy, N. Kumar, P. V. Bernhardt, D.R. Richardson, Design, synthesis, and characterization of novel iron chelators: structure-activity relationships of the 2-benzoylpyridine thiosemicarbazone series and their 3-nitrobenzoyl analogues as potent antitumor agents, J Med Chem 50 (2007) 3716–3729.
[27] Z. Debebe, T. Ammosova, M. Jerebtsova, J. Kurantsin-Mills, X. Niu, S. Charles, D. R. Richardson, P.E. Ray, V.R. Gordeuk, S. Nekhai, Iron chelators ICL670 and 311 inhibit HIV-1 transcription, Virology 367 (2007) 324–333.
[28] Z. Debebe, T. Ammosova, D. Breuer, D.B. Lovejoy, D.S. Kalinowski, K. Kumar, M. Jerebtsova, P. Ray, F. Kashanchi, V.R. Gordeuk, D.R. Richardson, S. Nekhai, Iron chelators of the di-2-pyridylketone thiosemicarbazone and 2-benzoylpyridine thiosemicarbazone series inhibit HIV-1 transcription: identification of novel cellular targets–iron, cyclin-dependent kinase (CDK) 2, and CDK9, Mol Pharmacol 79 (2011) 185–196.
[29] G.M. Sheldrick, SHELXT - integrated space-group and crystal-structure determination, Acta Crystallogr A Found Adv 71 (2015) 3–8.
[30] G.M. Sheldrick, A short history of SHELX, Acta Crystallographica Section A: Foundations 64 (2008) 112–122.
[31] G.M. Sheldrick, Crystal structure refinement with SHELXL, Acta Crystallographica Section C: Structural Chemistry C71 (2015) 3–8.
[32] O.V.B. Dolomanov, R.J.Gildea LJ, J.A.K. Howard, H. Puschmann, OLEX2: a complete structure solution, refinement and analysis program, J Appl Crystallogr 42 (2009) 339–341.
[33] D.F. de Lima, A. Pérez-Rebolledo, J. Ellena, H. Beraldo, 2-Benzoyl-pyridine semicarbazone, Acta Crystallogr Sect E Struct Rep Online 64 (2007) o177.
[34] J.M. Myers, Q. Cheng, W.E. Antholine, B. Kalyanaraman, A. Filipovska, E.S. Arnér, C.R. Myers, Redox activation of Fe(III)-thiosemicarbazones and Fe(III)-bleomycin by thioredoxin reductase: specificity of enzymatic redox centers and analysis of reactive species formation by ESR spin trapping, Free Radic Biol Med 60 (2013) 183–194.
[35] A. Fathy, A.B.M. Ibrahim, S.A. Elkhalik, A. Villinger, S.M. Abbas, New iron(III) complexes with 2-formylpyridine thiosemicarbazones: synthetic aspects, structural and spectral analyses and cytotoxicity screening against MCF-7 human cancer cells, Heliyon 9 (2023) e13008.
[36] I. Doumi, L. Lang, B. Vileno, M. Deponte, P. Faller, Glutathione protects other cellular thiols against oxidation by Cu^{II}-Dp44mT, Chemistry (Easton) 30 (2024) e202304212.
[37] E.W. Hunsaker, K.J. Franz, Emerging opportunities to manipulate metal trafficking for therapeutic benefit, Inorg Chem 58 (2019) 13528–13545.
[38] A. Frei, J. Zuegg, A.G. Elliott, M. Baker, S. Braese, C. Brown, F. Chen, C.G. Dowson, G. Dujardin, N. Jung, A.P. King, A.M. Mansour, M. Massi, J. Moat, H.A. Mohamed, A.K. Renfrew, P.J. Rutledge, P.J. Sadler, M.H. Todd, C.E. Willans, J.J. Wilson, M. A. Cooper, M.A.T. Blaskovich, Metal complexes as a promising source for new antibiotics, Chem Sci 11 (2020) 2627–2639.
[39] D.J. Lane, T.M. Mills, N.H. Shafie, A.M. Merlot, R. Saleh Moussa, D.S. Kalinowski, Z. Kovacevic, D.R. Richardson, Expanding horizons in iron chelation and the treatment of cancer: role of iron in the regulation of ER stress and the epithelial-mesenchymal transition, Biochim Biophys Acta 1845 (2014) 166–181.